Chemical Science

ROYAL SOCIETY OF CHEMISTRY

EDGE ARTICLE

View Article Online
View Journal | View Issue



Cite this: *Chem. Sci.*, 2023, **14**, 10112

All publication charges for this article have been paid for by the Royal Society of Chemistry



# Dimeric tetrabromo-*p*-quinodimethanes: synthesis and structural/electronic properties†

Diego J. Vicent, ‡[a] Manuel Pérez-Escribano, ‡[b] Abel Cárdenas-Valdivia,[c] Ana Barragán, [d] Joaquín Calbo, [b] José I. Urgel, [d] David Écija, *[d] José Santos, *[a] Juan Casado, *[c] Enrique Ortí *[b] and Nazario Martín *[ad]

Despite their great potential as molecular building blocks for organic synthesis, tetrabromo-*p*-quinodimethanes (**TBQ**s) are a relatively unknown family of compounds. Herein, we showcase a series of five derivatives incorporating two tetrabromo-anthraquinodimethane (**TBAQ**) units linked by π-conjugated spacers of different nature and length. The resulting dimers **TBQ1–5** are fully characterised by means of thorough spectroscopic measurements and theoretical calculations. Interestingly, owing to the steric hindrance imposed by the four bulky bromine atoms, the **TBAQ** fragments adopt a characteristically warped geometry, somehow resemblant of a butterfly, and the novel dimers show a complex NMR pattern with signal splittings. To ascertain whether dynamic processes regarding fluxional inversion of the butterfly configurations are involved, first-principles calculations assessing the interconversion energy barriers are performed. Three possible stereoisomers are predicted involving two diastereomers, thus accounting for the observed NMR spectra. The rotational freedom of the **TBAQ** units around the π-conjugated linker influences the structural and electronic properties of **TBQ1–5** and modulates the electronic communication between the terminal **TBAQ** moieties. The role of the linker on the electronic properties is investigated by Raman and UV-vis spectroscopies, theoretical calculations and UV-vis measurements at low temperature. **TBQ1–5** are of interest as less-explored structural building precursors for a variety of scientific areas. Finally, the sublimation, self-assembly and reactivity on Au(111) of **TBQ3** is assessed.

Received 28th March 2023
Accepted 9th August 2023

DOI: 10.1039/d3sc01615c

rsc.li/chemical-science

## Introduction

Bottom-up synthetic approaches for preparing complex organic structures can be highly time and resources consuming. Thus, organic chemists tend to make use of pre-made molecular fragments, modularly assembling them into more complex structures. These so-called molecular building blocks are usually endowed with different reactive functional groups supported onto a scaffold of low-to-medium complexity. The use of appropriate building blocks, therefore, allows speeding up the synthetic tasks as well as decreasing the synthetic costs.

Molecules bearing *gem*-dibromoolefine functionalities have been employed as intermediates in the well-known Ramirez–Corey–Fuchs homologation of carbonyls to alkynes.[1,2] They are readily attained from either ketones or aldehydes by reacting with carbon tetrabromide and triphenylphosphine. Upon lithiation, *gem*-dibromoolefines undergo Fritsch–Buttenberg–Wiechell (FBW) rearrangement to yield the corresponding alkyne.[3,4] Besides their use in FBW rearrangements, this functionality has found use in the synthesis of [4]radialene.[5] Nonetheless, it is as substrates for palladium cross-coupling reactions where *gem*-dibromoolefines have found a broader use, allowing Suzuki,[6] Stille[7] and Sonogashira couplings.[8] When the *gem*-dibromoolefines are stemming from *p*-quinones, the resulting tetrabromo-*p*-quinodimethanes (**TBQ**s) may undergo dehalogenative homocoupling on coinage metal surfaces, namely Au(111) and Ag(111), forming one-dimensional (1D) acene and periacene polymers that may exhibit appealing non-trivial topological electronic properties, depending upon the acene nature and length of the polymer.[9–13]

As building blocks bearing four reactive bromine atoms, **TBQ**s are excellent platforms for the incorporation of up to four substituents. This high degree of functionalisation is ideal for some organic electronics applications, as in the case of hole

[a]*Departamento de Química Orgánica, Facultad de Ciencias Químicas, Universidad Complutense de Madrid, 28040 Madrid, Spain. E-mail: jsantosb@pdi.ucm.es; nazmar@quim.ucm.es*

[b]*Instituto de Ciencia Molecular, Universidad de Valencia, 46980 Paterna, Spain. E-mail: enrique.orti@uv.es*

[c]*Departamento de Química Física, Universidad de Málaga, 229071 Malaga, Spain. E-mail: casado@uma.es*

[d]*IMDEA-Nanociencia, C/ Faraday, 9, Campus de Cantoblanco, 28049 Madrid, Spain. E-mail: david.ecija@imdea.org*

† Electronic supplementary information (ESI) available. See DOI: https://doi.org/10.1039/d3sc01615c

‡ These authors contributed equally to the work.

transporting materials (HTMs) for perovskite solar cells (PSCs), where the presence of several electroactive arylamine groups strongly enhances the charge transport. For instance, when triarylamine functionalities are inserted into an anthraquinone-based **TBQ** (**TBAQ**), the resulting HTM exhibits high photovoltaic performance and stability in large area PSCs.[14] The steric hindrance of the anthracene *peri* hydrogens allows conceiving molecules with switchable geometry, which makes **TBQ**s ideal platforms for synthetising materials with aggregation-induced emission (AIE) and photochromism properties.[15–17] If the core of the **TBQ** is a pentacene, then the substitution with phenyl derivatives yields a structure that is prone to undergo a cyclodehydrogenation reaction to provide hexabenzocoronenes, which have potential as semiconducting materials for field-effect transistor applications.[18] Another example of their potential in materials science is found in molecules with self-assembly capabilities.[19]

Regarding their chemical structure, **TBQ** building blocks can be considered as precursors for the synthesis of π-extended analogues of Thiele's and Chichibabin's hydrocarbons. Owing to their quinoid character, they have a strong tendency to stabilise open-shell chemical structures when suitably substituted.[20,21] For example, the deposition of a bipentacene **TBQ** on a Au(111) surface allowed the synthesis of peripentacene and the unequivocal characterization of its open-shell character.[22]

The versatility of the **TBQ** functionality as building block for preparing a wide variety of molecules of high interest in materials science and organic electronics prompted us to design, synthesise and expand the spectrum of **TBQ** derivatives by preparing a series of anthracene-based **TBQ** dimers (Scheme 1). The newly synthesised **TBQ1–5** molecules are endowed with eight bromine atoms located on the two anthra-*p*-quinodimethane units which are, in turn, covalently connected by different spacers that modulate the conjugation and/or electronic communication between them. The structural, electronic, optical and vibrational experimental properties of the **TBAQ** building block and of the **TBQ** dimers were jointly studied with first-principles calculations and spectroscopic techniques to deepen into the understanding of their intramolecular characteristics. Furthermore, the sublimation, self-assembly and reactivity of a **TBQ** archetype (**TBQ3**) was explored on Au(111). Altogether, our findings could eventually seed supramolecular and material properties based on these high-bromine functional molecules.

## Results and discussion

### Synthesis and structural properties

The synthesis of **TBQ**-based building blocks can be achieved starting from relatively unexpensive products (Scheme 1). Reaction of 4,4′-oxydiphthalic anhydride (**1**) with $AlCl_3$ in benzene, followed by treatment of the resulting product with polyphosphoric acid (PPA) provides anthraquinone dimer **2** in good yield.[23] To obtain **TBQ1**, standard Ramirez olefination conditions employing $CBr_4$ and $PPh_3$ were applied,[1] although the yields were low to moderate. On the other hand, to synthesise **TBQ2–5** the key starting material was 2-bromoanthraquinone (**3**), which may be purchased from commercial retailers or readily attained from bromobenzene and phthalic anhydride. Product **TBQ2** is obtained starting from **3** in two steps. First step involves the one-pot two-fold Sonogashira cross-coupling of trimethylsilylacetylene with two molecules of **3**, enabled by the use of 1,8-diazabicyclo[5.4.0]undec-7-ene (DBU) as base, with moderate yield. When the resulting acetylene-bridged anthraquinone dimer (**4**) is exposed to standard Ramirez olefination conditions, inseparable complex reaction mixtures were obtained. The study of the crudes by mass spectroscopy revealed peaks with isotopic profiles compatible with molecules carrying various bromine atoms. Following a previous study by M. Lauten and coworkers,[24] where phosphites demonstrated enhanced reactivity towards ketones compared to phosphines, tri-iso-propylphosphite [$P(OiPr)_3$] was employed. Use of 2 and 4 equivalents of $CBr_4$ and $P(OiPr)_3$, respectively, per carbonyl equivalent, led to partial olefination products of **4**, although no complex mixtures were observed.

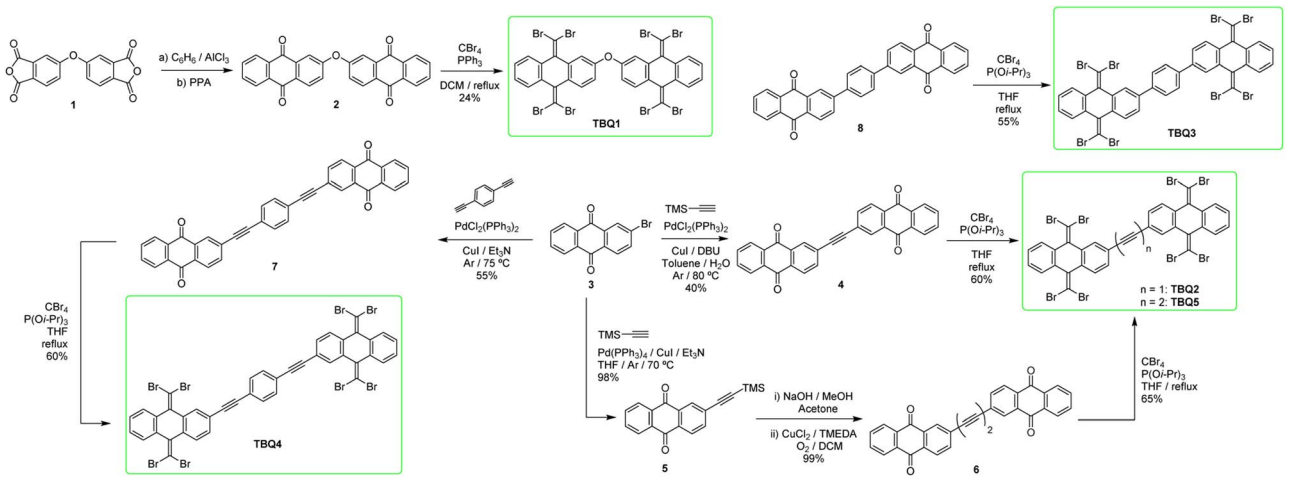


Scheme 1 Synthetic route to the dimeric tetrabromo-*p*-quinodimethanes TBQ1–5.

Full conversion of the starting material to **TBQ2** was finally achieved by adding three extra loads of $CBr_4$ and $P(OiPr)_3$.

To synthesise **TBQ5** from precursor **6**, featuring a butadiyne bridge, 2-ethynylanthraquinone was quantitatively homo-coupled *via* Hay coupling. For preparing **TBQ4** from precursor **7**, the starting material **3** was coupled with 1,4-diethynylbenzene by Sonogashira reaction. Finally, precursor **8** used to obtain **TBQ3** was prepared by Suzuki reaction of **3** with 1,4-bis(4,4,5,5-tetramethyl-1,3,2-dioxaborolan-2-yl)benzene. Final products **TBQ3–5** were obtained following the same procedure as for **TBQ2** (Scheme 1). The FTIR spectra of **TBQ1–5** evidence the lack of the characteristic carbonyl band of the precursing quinones, along with the arising of an intense sharp band at *ca.* 760 $cm^{-1}$ ascribed to the out-of-plane bending of the C=$CBr_2$ moieties. Featuring eight bromine atoms per molecule, **TBQ1–5** show a very characteristic isotopic profile (see Fig. S13–S19†).

Prior to theoretically characterizing the high-bromine **TBQ1–5** dimers, the structure of the **TBAQ** building block was inspected and compared with that computed for the widely studied cyano-based tetracyanoanthra-*p*-quinodimethane (**TCAQ**) analogue. Geometry optimizations were performed within the density functional theory (DFT) framework at the BMK/6-31G(d,p) level of theory in gas phase (see the Computational methods section in the ESI† for full computational details and methodology benchmark). In the case of **TCAQ**, the fully planar $D_{2h}$ conformation is a high-order saddle point with four imaginary vibrational modes (see Section S6 in the ESI†).[25–27] When considering **TBAQ**, the $D_{2h}$ conformation shows up to five imaginary vibrational frequencies (Section S7†). Starting from this planar structure, the search for the global minimum-energy conformer was performed by distorting the molecular geometry along the imaginary vibrational modes with symmetry constraints (Fig. 1). Three conformations, two of them equivalent to each other and possessing a $C_{2h}$ point group of symmetry ($C'_{2h}$ and $C^*_{2h}$), and the $D_2$ conformation, are transition states and a high-order saddle point, respectively, that further present one or two imaginary frequencies. These three structures are calculated *ca.* 20 kcal $mol^{-1}$ more stable than the planar $D_{2h}$ molecular geometry. From the $D_2$ conformation, a local minimum-energy, chair-like structure is predicted with no imaginary frequency and $C_{2h}$ symmetry, which is computed 31.3 kcal $mol^{-1}$ more stable than the $D_{2h}$ conformer (Fig. 1). Finally, the global minimum-energy structure, displaying a saddle- or butterfly-like disposition, belongs to the $C_{2v}$ point group of symmetry, and is calculated 53.8 kcal $mol^{-1}$ lower in energy than the planar $D_{2h}$ structure. Noticeably, the butterfly inversion through $D_{2h}$ is highly unfavorable for **TBAQ** (53.8 kcal $mol^{-1}$) compared to **TCAQ** (22.3 kcal $mol^{-1}$). However, as the intermediate transition states ($C'_{2h}$, $C^*_{2h}$ and $D_2$) connect with the $C_{2v}$ global minimum, the butterfly shape of **TBAQ** can be inverted with an activation barrier of 33.3 kcal $mol^{-1}$, to be compared with a value of 18.4 kcal $mol^{-1}$ for **TCAQ**. Nonetheless, the butterfly interconversion process is still significantly impeded at room temperature.

To gain insight into the structural changes driving the relative energy difference between the $C_{2v}$ global minimum-energy structure and the planar $D_{2h}$ transition state for **TBAQ** in comparison to **TCAQ**, we investigated the two main structural deformations that follow the interconversion from $D_{2h}$ to $C_{2v}$; *i.e.*, the planar-to-butterfly change and the widening of the Br–C–Br and NC–C–CN bond angles (see Section S8† for details). Theoretical calculations at the BMK/6-31G(d,p) level indicate that the change from planar to butterfly shape, in going from $D_{2h}$ to $C_{2v}$, leads to a net stabilization of −37.4 and −10.7 kcal $mol^{-1}$ for **TBAQ** and **TCAQ**, respectively. The larger stabilization observed for **TBAQ** is consistent with the presence of the bulkier Br atoms, compared to the cyano groups of **TCAQ**, as the electron localization function evidences (Fig. S25†).[28] In line with the previous reasoning, in **TBAQ** the broadening of the Br–C–Br angle from 98° in $D_{2h}$ to 124° in $C_{2v}$ provides a larger stabilization (−16.1 kcal $mol^{-1}$) than the relaxation of the NC–C–CN angle of **TCAQ** (from 97° in $D_{2h}$ to 111° in $C_{2v}$ with a stabilization of −11.1 kcal $mol^{-1}$), thus supporting the larger steric interactions between Br atoms.

The $^1H$ and $^{13}C$ magnetic resonances of the **TBQ1–5** dimers reveal interesting structural aspects of these molecular systems (Fig. S3–S12†). Considering the substitution pattern of the phenyl rings through which the anthracenes are linked by (Scheme 1), the $^1H$-NMR spectra should show three sets of

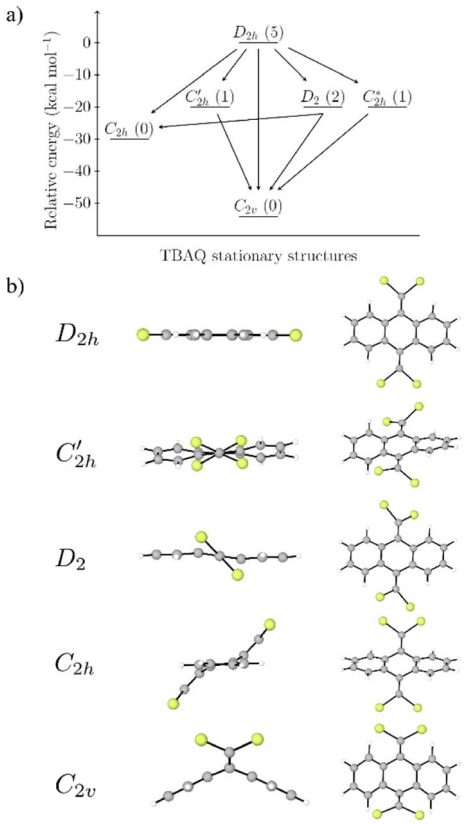


Fig. 1 Relative electronic energy (a) and molecular structure (b) of the different conformations localized at the BMK/6-31G(d,p) level on the potential energy surface of TBAQ. In (a), the number of imaginary frequencies of each structure is indicated within parentheses, and the arrows indicate the evolution of the structure upon deformation along the imaginary modes. In (b), side (left) and top (right) views are displayed. Color coding: H in white, C in gray and Br in yellow.

signals integrating for one proton each: the lone *peri* proton (position C1) showing as a doublet, coupled with a small $^4$J coupling constant to the proton in *meta* (position C3); the latter appearing as a double doublet due to the coupling with the proton in *ortho* to it (position C4); this last proton showing itself as a doublet. Instead, some of these signals split in some of the **TBQ**s, *i.e.*, H–C1 and H–C3 of **TBQ1** (Fig. S3†) and **TBQ2** (Fig. 2). In the case of these dimers bearing shorter linkers, the proximity of both **TBAQ** subunits seems to create different magnetic environments for the above-mentioned protons. As larger spacers are introduced, *e.g.* in **TBQ5**, the splitting effect tends to vanish, as both **TBAQ**s stop magnetically affecting each other (see Fig. 2). The splitting effect is also observed in the case of the $^{13}$C-NMR signals, mainly concerning the signal of the carbon nuclei involved in the alkyne fragment and the ones close to it (C1, C2 and C3) (see Fig. S4, S6 and S9†).

In order to assess the possibility of having rotamers with different butterfly-to-butterfly relative orientations (same *vs.* opposite orientation with respect to the molecular plane) that may explain the NMR signal splitting described above, the energy barrier for single-bond **TBAQ** rotation was evaluated for **TBQ1–5** dimers at the BMK/6-31G(d,p) level including solvent conditions ($CH_2Cl_2$) (see Section S9 of the ESI† for further details). Fig. 3 displays the rotational barrier profile calculated for **TBQ2** as a representative example (see Fig. S26–S29† for the other dimers). Theoretical calculations indicate that the butterfly rotation along dihedral angle $\theta$ is accessible at room temperature, as torsion barriers in the range of 0.31–3.47 kcal mol$^{-1}$ are predicted for the highly containing bromine dimers (Table S2†). The largest energy barriers are predicted for **TBQ1** and **TBQ3** due to the evident H···H steric hindrance upon rotation. Analysis of the Br···H–C1 distance (Fig. S30†) confirms a significant change in length upon butterfly rotation (Table S3†). This distance is significantly shorter for **TBQ1** and **TBQ2**, achieving minimum values of 5.12 and 6.17 Å, respectively, which could explain the $^1$H-NMR signal splitting recorded experimentally for the H–C1 *peri* proton in these derivatives bearing shorter linkers (Fig. 2).

A detailed analysis of the possible configurational isomers of **TBQ2** (Fig. S1†) reveals the presence of three possible isomers,

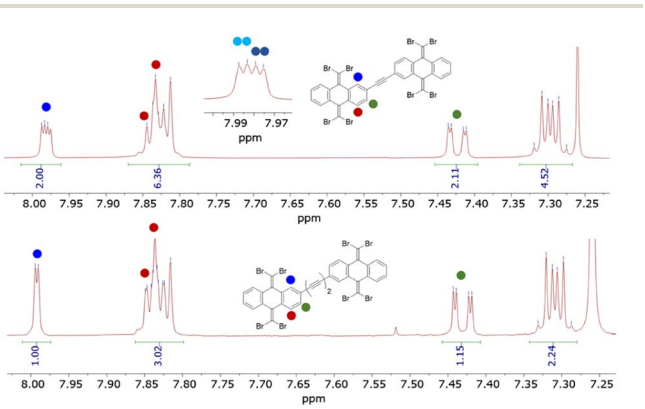


Fig. 2 Comparison of the $^1$H-NMR spectra of **TBQ2** and **TBQ5** showing the splitting of the *peri* hydrogen signal of the former, consistent with the presence of two isomeric species.

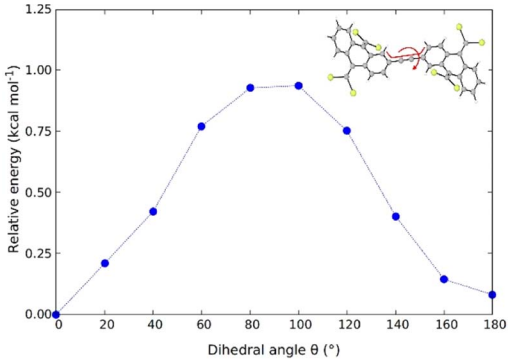


Fig. 3 Rotational energy barrier profile calculated for **TBQ2** at the BMK/6-31(d,p)+PCM($CH_2Cl_2$) level along the torsion of the dihedral angle $\theta$ (in red) defining the relative orientation of the **TBAQ** moieties.

*i.e.*, a pair of enantiomers and a *meso* form. Attempts to isolate the diastereomers by chromatographic means were to no avail due to the limited solubility of **TBQ2** in the eluting mixture and the negligible chromatographic separation between diastereomers. However, $^1$H-NMR spectra of the collected fractions show diminished intensity for one of the doublets constituting the split signal of the H–C1 *peri* proton (see Fig. S12†), as would be expected from a fraction enriched in one of the diastereomers.

## Vibrational spectroscopic properties

The solid-state Raman spectra of the **TBQ** dimers together with that recorded for **TBAQ** are shown in Fig. 4a. The BMK/6-31G(d,p) Raman spectrum simulated for **TBQ2** compares very well with the experimental spectrum in the whole spectral region, as may be observed in Fig. S63,† allowing to make a vibrational assignment of the experimental bands in terms of the main components of the vibrational normal modes (Fig. S64 and S65†). The experimental bands of **TBQ2** at 1601 and 1593 cm$^{-1}$ can be correlated with the theoretical bands at 1593 and 1579 cm$^{-1}$, respectively. The two modes are composed by the C=C stretching modes [$\nu$(C=C)] of the anthraquinone core with CC displacements featuring the breathing mode of the six-member rings (*i.e.*, vibrational normal modes **1** and **3** of benzene, see Fig. 4b) and coupled with the outermost methylene C=C stretches of the $CCBr_2$ moieties, or $\nu(C{=}C)_{mode1\text{-}3}$ + $\nu(C{=}CBr_2)$. On the other hand, the experimental bands of **TBQ2** at 1582 and 1561 cm$^{-1}$ correspond to those theoretically predicted at 1569 and 1553 cm$^{-1}$, respectively, and can be described as C=C stretching modes carrying out the **8a** mode of benzene in which the bonds of the central six-member ring, which are parallel to the external methylene double bonds, simultaneously stretch, or $\nu(C{=}C)_{mode8}$ + $\nu(C{=}CBr_2)$. The BMK/6-31G(d,p) theoretical Raman spectra calculated for **TBAQ** at the $C_{2v}$, $C_{2h}$ and $D_{2h}$ geometries in Fig. 1 (Fig. S66†) reveals that the $\nu$(C=C) + $\nu(C{=}CBr_2)$ bands experience a progressive increment of their wavenumbers upon sequential $C_{2v} \rightarrow C_{2h} \rightarrow D_{2h}$ planarization of the central anthracene core.

The experimental vibrational Raman intensity patterns of **TBQ2** and **TBAQ** in the 1600 cm$^{-1}$ region are apparently very similar, the wavenumbers of the corresponding bands showing

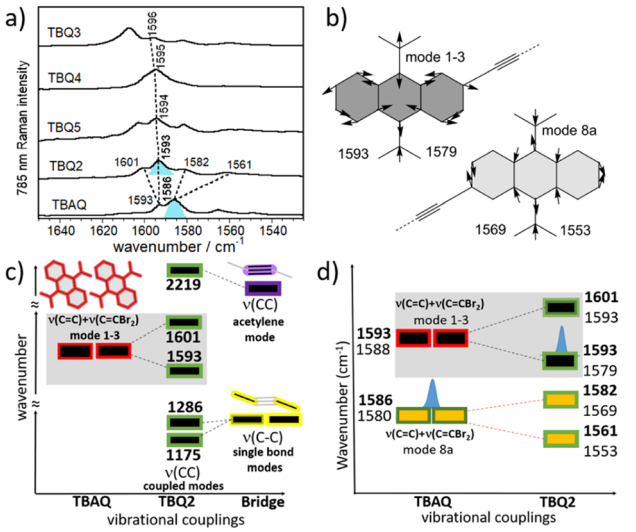


Fig. 4 (a) Raman spectra of the compounds in solid state at 298 K, employing a 785 nm laser (blue-shaded bands are those mainly discussed in the text). (b) BMK/6-31G(d,p) theoretical vibrational $\nu$(CC) modes (wavenumbers in cm$^{-1}$) of **TBQ2** showing the main CC displacements and related to the modes *1, 3* and *8a* of benzene. (c) Wavenumber evolution of the $\nu$(CC) vibrational modes (mode *1–3* of benzene) from the **TBAQ** units (in red) upon vibrational coupling with the central $\nu$(CC) acetylene spacer (in purple) and with the $\nu$(CC) of the single connecting bonds (in yellow). Vibrational splittings are qualitative. (d) Vibrational splitting of the *1–3* and *8a* modes simultaneously from **TBAQ** to **TBQ2**. Experimental values are shown in bold (blue-shaded bands are those equally denoted in the experimental spectra).

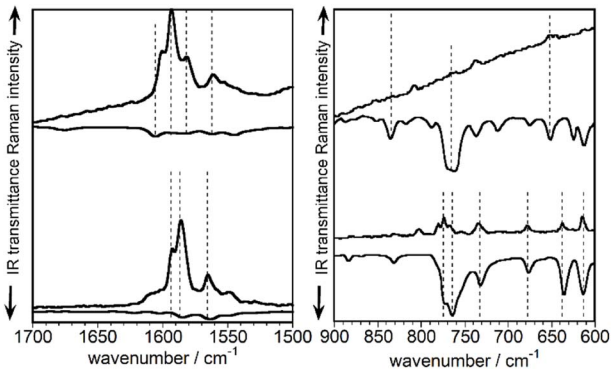


Fig. 5 Comparison between the 785 nm solid-state laser Raman (pointing up) and the infrared (pointing down) spectra of **TBAQ** (below) and **TBQ2** (above) at 298 K, normalized to the strongest Raman and infrared bands.

an overall upshift in passing from **TBAQ** to **TBQ2** (Fig. 4a). For instance, the strongest Raman band at 1586 cm$^{-1}$ in **TBAQ** shifts to 1593 cm$^{-1}$ in **TBQ2** (blue-shaded in Fig. 4a). This strong band keeps slightly upshifting in the dimers, up to by +3 cm$^{-1}$ on **TBQ2** → **TBQ3**. There are two possible reasons behind these wavenumber upshift upon dimerization: (i) the planarization of the anthracene core, as observed for **TBAQ** along $C_{2v}$ → $C_{2h}$ → $D_{2h}$ symmetry transformations (Fig. S66†), and (ii) the role of the linker in the dynamics and electronic structure of the **TBAQ** units upon formation of **TBQ2**. Comparison of the optimized minimum-energy geometries calculated for the **TBAQ** molecule and the **TBAQ** subunits within the dimers indicates a negligible planarization of the butterfly moiety in **TBQ1–5**, with root-mean-square deviations of the atomic positions in the dimers with respect to **TBAQ** smaller than 0.01 Å and a folding of the anthracene skeleton differing in only 0.2° (Table S4†). On the other hand, the vibrational couplings suggested in point (ii) are qualitatively presented in Fig. 4c and d (and Fig. S64 and S65†), where the evolution of the $\nu$(CC) modes upon assembly and subsequent vibrational mixing of two **TBAQ** monomers with a central acetylene (and with two CC single bonds) is shown. The **1–3** and **8a** benzenoid-like modes of **TBAQ** are calculated at 1588 and 1580 cm$^{-1}$, respectively, in good correlation with the Raman peaks observed at 1593 and 1586 cm$^{-1}$. Interestingly, in the theoretical Raman spectra of **TBAQ** and **TBQ2**, the most active Raman bands correspond to modes of different vibrational nature, the **8a** mode in **TBAQ** at 1580 cm$^{-1}$ and the **1–3** mode in **TBQ2** at 1579 cm$^{-1}$. This change in the vibrational structure of the strongest Raman bands reveals the effect of the dimerization in the vibrational spectra, which modifies the electronic polarizability tensor in such a way that its largest variation between **TBAQ** and **TBQ2** occurs in different vibrational modes. Elongation of the bridge between the two **TBAQ** units in compounds **TBQ3–5** slightly modifies the vibrational mixing and similar frequencies are detected in the Raman spectra. Conversely, vibrational bands of the same nature are found to downshift upon dimerization, what is in accordance with the common finding that the Raman wavenumbers always decrease with the increment of π-conjugation in oligomeric series.[29–31]

Fig. 5 displays the normalized infrared and Raman spectra of **TBAQ** and **TBQ2** in the spectral regions where the strongest bands are measured, *i.e.*, around 1600 cm$^{-1}$ for the $\nu$(CC) modes in the Raman spectrum and at 750 cm$^{-1}$ for the $\nu$(CBr) modes in the infrared spectrum (theoretically compared in Fig. S67 and S68†). In general, for the two molecules under comparison and concerning their vibrational bands in common (*i.e.*, those of **TBAQ**), it can be seen that each strong Raman band around 1600 cm$^{-1}$ has a weak infrared analogue feature. Conversely, in the region around 750 cm$^{-1}$, each intense infrared band has a corresponding weak Raman feature. This reveals that all these vibrations display non-vanishing infrared and Raman intensities, which is in agreement with a $C_{2v}$ molecular symmetry in **TBAQ** and a local $C_{2v}$ conformation for the **TBAQ** units in **TBQ2** as well. Nonetheless, it is observed in Fig. 5 that every Raman (infrared) active mode of **TBQ2** is much less active in the infrared (Raman) (dotted lines correlate vibrational modes in the Raman and infrared spectra) than the corresponding signals in **TBAQ**. This observation might be indicative of a symmetry alteration upon formation of the dimer, whose molecular structure evolves closer to a form with an inversion centre around the central acetylene bridge.

## Electronic structure and optical properties

The electronic structure of the high-bromine dimers **TBQ1–5** was studied at the DFT-BMK/6-31G(d,p) level in

dichloromethane. Theoretical calculations indicate that the highest-occupied molecular orbital (HOMO) is mainly delocalized over the bridge and the inner benzene ring of the anthraquinone moieties (see Fig. S31†). Similarly, the lowest-unoccupied molecular orbital (LUMO) is centred over the bridge and extends to the **TBAQ** moieties, especially for the less conjugated **TBQ1** and **TBQ3** derivatives. Increasing the π-conjugation of the bridge leads to a systematic destabilization of the HOMO level from −6.81 eV in **TBQ1** to −6.43 eV in **TBQ4**, whereas the LUMO lowers in energy from −1.34 eV in **TBQ1** to −1.82 eV in **TBQ5** (Table S5†). As a result, the HOMO–LUMO energy gap varies in a range of values from 5.47 eV for **TBQ1** to 4.69 eV for **TBQ4**, suggesting a strong shift in the optical properties along the family of **TBQ** dimers (see below).

The large destabilization of the LUMO of **TBAQ** (−1.18 eV) and **TBQ** dimers (from −1.34 to −1.82 eV, Table S5†) compared to **TCAQ** (−3.49 eV) remarks that the reduction of the **TBAQ** moiety is significantly hindered compared to **TCAQ**. As a consequence, **TBQ1–5** show no reduction activity in the cyclic voltammetry experiments performed within the solvent scan window. It is noteworthy, that exocyclic bromovinylenes are prone to decomposition *via* debromination, thus limiting the experimental characterization of their redox properties.

The experimental optical characterisation of **TBQ1–5** is summarized in Fig. 6. All **TBQ** dimers present absorption features in the UV region between 250 and 370 nm. The lowest energy absorption of **TBQ1** (300 nm) and **TBQ3** (314 nm) is blue shifted compared to the other **TBQ**s, due to the restricted conjugation imposed by their oxygen and phenyl linkers. When an alkyne linker is introduced in **TBQ2**, extension of the conjugation effect is evidenced by a red shift of the absorption (349 nm). Increasing the length of the π-conjugated bridge leads to lower-energy absorptions in **TBQ4** and **TBQ5** (368 and 365 nm, respectively). Interestingly, the dimers with alkyne spacers (**TBQ2** and **TBQ5**) show similar absorption profiles featuring four bands, the most energetic two lying at *ca.* 263 and 315 nm, and the lower-energy ones peaking at 325 and 349 nm for **TBQ2** and 339 and 365 nm for **TBQ5**. All **TBQ** derivatives exhibit weak emission features in non-deaerated solutions, with small Stokes shifts of about 10 nm for **TBQ2**, **TBQ4** and **TBQ5**, and 30 and 55 nm for **TBQ1** and **TBQ3**, respectively.

Theoretical calculations were performed by means of the time-dependent DFT (TD-DFT) approach to unveil the nature of the low-lying absorption bands for **TBQ1–5**. The lowest-energy absorption band experimentally recorded at 300–365 nm results from the electronic transition to the first singlet excited state $S_1$ (Fig. S33–S37†), except for **TBQ1**, for which the transition to the $S_2$ state is predicted near $S_1$ and also contributes to this band with an oscillator strength (*f*) of 0.551 (Fig. S33†). The $S_0 \rightarrow S_1$ transition mostly originates in the HOMO → LUMO monoexcitation (Table S6†), and, according to the topology of these orbitals, is described by a local excitation mainly centred in the linker and the inner anthraquinone halves. The electronic nature of the $S_1$ excitation is confirmed by the natural transition orbitals involved in the transition (Fig. S38–S42†),[32] which suggest a small charge-transfer from the linker to the **TBAQ** moieties, especially for the less-conjugated **TBQ1** and **TBQ3** derivatives.

The effect of the internal rotation of the **TBAQ** units on the first singlet excited states was disclosed to better understand the complex low-lying absorption pattern with several peaks recorded for **TBQ2** and **TBQ5** (Section S13†). TD-DFT calculations indicate that the torsion of the **TBAQ** moiety along $\theta$ significantly shifts the $S_1$ excitation energy, *e.g.*, from 335 nm at $\theta = 0°$ to 300 nm at $\theta = 100°$ for **TBQ2** (Fig. S43†). The torsion also impacts on the position and intensity of higher-energy states as predicted for the excited states $S_2$ and $S_4$ of **TBQ5** at intermediate rotation angles ($\theta$ = 80–100°, Fig. S45†). These results highlight that the position of the absorption peaks recorded experimentally and the shape of the absorption spectra, especially in **TBQ2** and **TBQ5**, might come from the large rotational freedom of these **TBQ** dimers.

The study of the evolution of the absorption features of **TBQ2** as a function of the temperature on cooling (Fig. 7) reveals progressive spectral changes that mainly involve: (i) the red-shift of the absorption features, which is characteristic of π-conjugated chromophores, and (ii) a hyperchromic shift of the lowest-energy bands of the spectrum (*i.e.*, the band at 349 nm red shifts to 355 nm and becomes the strongest of the spectrum at 80 K). In addition, the resolution of new vibronic bands is observed, such as the 333/339 nm pair. This temperature-dependent behaviour is typically found in flexible π-

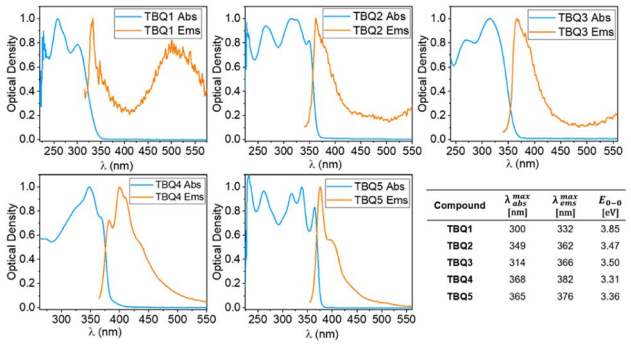


| Compound | $\lambda_{abs}^{max}$ [nm] | $\lambda_{ems}^{max}$ [nm] | $E_{0-0}$ [eV] |
|---|---|---|---|
| TBQ1 | 300 | 332 | 3.85 |
| TBQ2 | 349 | 362 | 3.47 |
| TBQ3 | 314 | 366 | 3.50 |
| TBQ4 | 368 | 382 | 3.31 |
| TBQ5 | 365 | 376 | 3.36 |

Fig. 6 Optical properties of **TBQ1–5** in $CH_2Cl_2$ solution at 25 °C. The blue plot corresponding to the normalised absorption and the orange to the normalised emission.

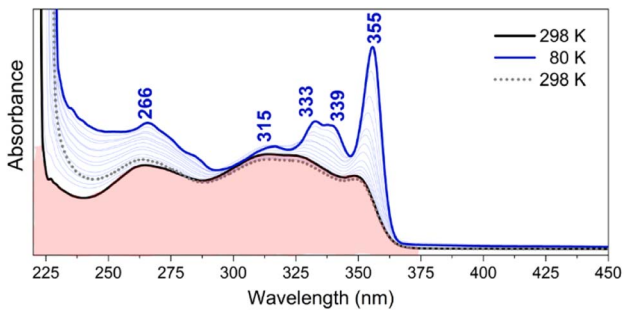


Fig. 7 Variable-temperature UV-vis electronic absorption spectra of **TBQ2** in 2-methyltetrahydrofurane upon cooling from 298 K to 80 K. The dotted grey line corresponds to the spectrum recorded at room temperature after cooling.

conjugated compounds, in which the blockade of the torsional vibrational motions produces a greater population of more planar conformers in detriment of the more distorted ones.[33] These conformationally frozen structures give way to the vibronic resolution and consequently the 0–0 vibronic bands become the most active bands of the spectrum.

The variable-temperature UV-vis experimental data are nicely supported by the rotational energy barriers obtained from quantum-chemical calculations. The predicted maximal energy barriers of *ca.* 1 kcal mol$^{-1}$ for **TBQ2** are assimilable to the amount of thermal energy removed on cooling from 298 to 80 K (*i.e.*, 0.43 kcal mol$^{-1}$). These results highlight that at room temperature the molecule has free rotation, with a broad set of thermally populated rotational conformers, whereas the rotation barrier becomes harder to overcome as the temperature diminishes. Therefore, only the most stable planar conformers are present at low temperature, and give rise to the vibronically-resolved UV-vis spectrum at 80 K.

### Self-assembly and reactivity on Au(111)

Finally, we have explored the capabilities of **TBQs** to steer molecular architectures on surfaces. To this aim, we deposited a submonolayer coverage of **TBQ3** on a pristine Au(111) surface kept at room temperature. As illustrated in Fig. 8a, after such deposition, a disordered molecular assembly is found, where characteristic bright protrusions coming in pairs are detected coexisting with irregular darker features. By a proper comparison with previous findings from our group, it is feasible to rationalize such molecular assembly.[9] **TBQ3** can be interpreted as two **TBAQ** units connected by a phenyl bridge. The deposition of **TBAQ** on Au(111) leads to a regular self-assembly in which the molecular species are intact, displaying a butterfly conformation and exhibiting two distinct adsorption geometries: either the phenyl moieties pointing up (observed in STM as two elongated bright protrusions) or down.[9] Similar results are visualized for the assembly of **TBQ3** on Au(111), though some of them appear in pairs. Thus, we rationalize that upon sublimation over 80% of **TBQ3** molecules cleave by the phenyl bridge, therefore **TBAQ** fragments coexist with pristine **TBQ3** on the surface. Importantly, adsorbed pristine **TBQ3** species (10–20%) are visualized as two consecutive pairs of two elongated protrusions, as illustrated in Fig. 8b.

Next, such molecular assembly was annealed to steer debromination and homocoupling reactions (Fig. 8c). We observed the formation of molecular wires, many of them corresponding to polymers arising from the homocoupling of debrominated **TBAQ** fragments. Notably, the surviving **TBQ3** species, from the sublimation and adsorption at room temperature, have been able to react upon annealing, giving rise to segments of conjugated ladder polymers, as illustrated in Fig. 8d, though featuring frequent side reactivity due to concomitant intra- and inter-molecular reactions.

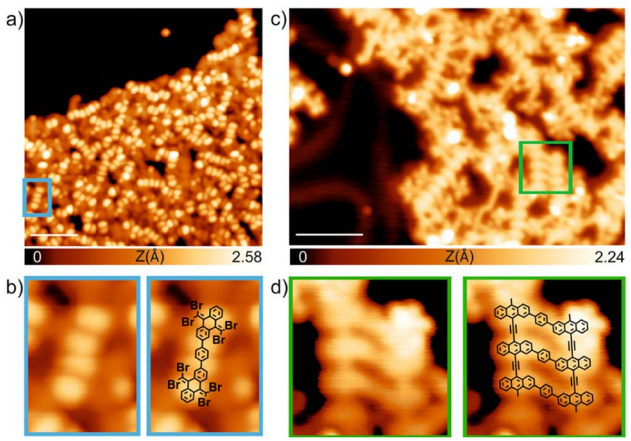


Fig. 8 On-surface deposition and reactivity of TBQ3 species on Au(111). (a) Overview STM image of the sublimation of a submonolayer coverage of TBQ3 on a pristine Au(111) surface kept at room temperature. $V_b = 1$ V, $I_t = 100$ pA, scale bar: 4.0 nm. (b) Left: Zoomed-in image of the blue rectangle indicated in panel (a) showing an intact molecule with two consecutive pairs of elongated bright protrusions. Right: Superposition of the chemical model. (c) Long-range STM image after the annealing of (a) at 150 °C. $V_b = 0.5$ V, $I_t = 50$ pA, scale bar: 4 nm. (d) Left: Zoomed-in image of the green highlighted area in panel (c). Right: Superposition of the chemical model.

## Conclusion

In summary, five novel dimeric molecules (**TBQ1–5**) based on the tetrabromoanthra-*p*-quinodimethane (**TBAQ**) motif have been synthesized. Owing to their high bromine content nature, these systems are excellent platforms for preparing more complex, highly substituted derivatives, which makes them very appealing and versatile building blocks. Theoretical DFT calculations reveal that the experimentally observed NMR signal splitting neither arise from slow rotation of the **TBAQ** moieties along the separating linker, nor from the fluxional inversion of the butterfly configuration of the **TBAQ** core. Featuring activation barriers in the 0.3–3.5 kcal mol$^{-1}$ range for bond rotation, **TBQ1–5** dimers can freely rotate at room temperature. On the other side, the high energy barriers predicted for the fluxional inversion of the butterfly configuration makes it unaffordable at low-to-moderate temperatures. Considering the characteristic butterfly geometry of the **TBAQ** subunits, when two such units are chemically bound, three possible stereoisomers involving a pair of enantiomers and a *meso* form are produced, thus explaining the observed NMR splitting. Interestingly, the Raman shifts to higher frequencies of the vibrational modes of **TBQ1–5** when increasing the length of the bridges linking the **TBAQ** moieties, point to an enhanced π-electron delocalization of the butterfly configuration of the **TBAQ**s, which is further evidenced in the electronic and optical properties. The modulation of such π-conjugation, even in small amounts, is a key aspect in the design of molecular building blocks and precursors given the enhancement or multiplicative effects these might have in the electronic structure of the final targeted products.

The preliminary on-surface chemistry study demonstrates the capabilities of **TBQ** species to be sublimated, adsorbed and homocoupled on surfaces, though still further research efforts are necessary to improve the sublimation and to promote the formation of regular polymers.

The results here reported unveil the structural, spectroscopic and electronic properties of these less-known but useful **TBAQ**-based building blocks and pave the way to a better understanding for the variety of further potential derivatives of interest in different scientific areas. Work is currently in progress in this regard.

## Data availability

The BMK/6-31G(d,p)(PCM)-optimized structures calculated for TBAQ, TCAQ and TBQ1-5 are available at the ZENODO repository (**https://doi.org/10.5281/zenodo.8038098**). Computational results and structures can also be retrieved from the authors upon request.

## Author contributions

N. M. and J. S. conceived the project. D. J. V., M. P.-E., A. C. V., and A. B. performed the investigation. J. S., M. P.-E., A. B., J. I. U., D. E., and J. C. analysed the results. J. S., M. P.-E, and J. C. wrote the manuscript. All authors reviewed and edited the manuscript. N. M., E. O. and J. C. supervised the project.

## Conflicts of interest

There are no conflicts of interest to declare.

## Acknowledgements

Financial support from the Spanish MCIN/AEI (projects PID2019-108532GB-I00, PID2020-114653RB-I00, PID2020-119748GA-I00, PID2021-127127NB-I00, PID2021-128569NB-I00, and TED2021-131255B-C44 funded by MCIN/AEI/10.13039/501100011033, Centro de Excelencia Severo Ochoa SEV-2016-0686, Unidad de Excelencia María de Maeztu CEX2019-000919-M and AEI/FEDER funds), the Comunidad de Madrid (project QUIMTRONIC-CM (Y2018/NMT-4783)), the Generalitat Valenciana (projects PROMETEO/2020/077 and MFA/2022/017), the Junta de Andalucía (PROYEXCEL-0328) and ERC-2020-SyG (Project: 951224) "TOMATTO" are acknowledged. This study was also supported by MCIN with funding from European Union NextGenerationEU (PRTR-C17.I1) (MAD2D-CM)-MRR project. M. P.-E. thanks grant PRE2021-097082 funded by MCIN/AEI and "ESF Investing in your future".

## Notes and references

1 N. B. Desai, N. McKelvie and F. Ramirez, *J. Am. Chem. Soc.*, 1962, **84**, 1745–1747.
2 E. J. Corey and P. L. Fuchs, *Tetrahedron Lett.*, 1972, **13**, 3769–3772.
3 S. Eisler, A. D. Slepkov, E. Elliott, T. Luu, R. McDonald, F. A. Hegmann and R. R. Tykwinski, *J. Am. Chem. Soc.*, 2005, **127**, 2666–2676.
4 W. A. Chalifoux and R. R. Tykwinski, *Nat. Chem.*, 2010, **2**, 967–971.
5 M. Iyoda, S. Tanaka, H. Otani, M. Nose and M. Oda, *J. Am. Chem. Soc.*, 1988, **110**, 8494–8500.
6 C.-Q. Chen, T. Chen, J.-X. Liu, G.-F. Zhang, C. Li, W.-L. Gong, Z.-J. Xiong, N.-H. Xie, B. Z. Tang and M.-Q. Zhu, *Macromolecules*, 2015, **48**, 7823–7835.
7 M. Shimizu, K. Nishimura, M. Mineyama and H. Fuji, *Org. Process Res. Dev.*, 2019, **23**, 1740–1745.
8 P. M. Donovan and L. T. Scott, *J. Am. Chem. Soc.*, 2004, **126**, 3108–3112.
9 A. Sánchez-Grande, B. de la Torre, J. Santos, B. Cirera, K. Lauwaet, T. Chutora, S. Edalatmanesh, P. Mutombo, J. Rosen, R. Zboril, R. Miranda, J. Björk, P. Jelínek, N. Martín and D. Écija, *Angew. Chem., Int. Ed.*, 2019, **58**, 6559–6563.
10 B. Cirera, A. Sánchez-Grande, B. de la Torre, J. Santos, S. Edalatmanesh, E. Rodríguez-Sánchez, K. Lauwaet, B. Mallada-Faes, R. Zbořil, R. Miranda, O. Gröning, P. Jelínek, N. Martín and D. Écija, *Nat. Nanotechnol.*, 2020, **15**, 437–443.
11 A. Sánchez-Grande, J. I. Urgel, A. Cahlík, J. Santos, S. Edalatmanesh, E. Rodríguez-Sánchez, K. Lauwaet, P. Mutombo, D. Nachtigallov, R. Nieman, H. Lischka, B. de la Torre, R. Miranda, O. Gröning, N. Martín, P. Jelínek and D. Écija, *Angew. Chem., Int. Ed.*, 2020, **59**, 17747–17752.
12 H. González-Herrero, J. I. Mendieta-Moreno, S. Edalatmanesh, J. Santos, N. Martín, D. Écija, B. de la Torre and P. Jelinek, *Adv. Mater.*, 2021, **33**, 2104495.
13 A. Sánchez-Grande, J. I. Urgel, I. García-Benito, J. Santos, K. Biswas, K. Lauwaet, J. M. Gallego, J. Rosen, R. Miranda, J. Björk, N. Martín and D. Écija, *Adv. Sci.*, 2022, **9**, 2200407.
14 G. Wu, Y. Zhang, R. Kaneko, Y. Kojima, A. Islam, K. Sugawa, J. Otsuki and S. Liu, *J. Power Sources*, 2020, **454**, 227938.
15 Z. He, L. Shan, J. Mei, H. Wang, J. W. Y. Lam, H. H. Y. Sung, I. D. Williams, X. Gu, Q. Miao and B. Z. Tang, *Chem. Sci.*, 2015, **6**, 3538–3543.
16 Y. Yin, H. Hu, Z. Chen, H. Liu, C. Fan and S. Pu, *Dyes Pigm.*, 2021, **184**, 108828.
17 J. Li, L. Gao, T. Lu, Z. Feng, D. Jiang, C. Du, K. Wang, P. Lu and B. Zou, *Adv. Opt. Mater.*, 2021, **9**, 2100813.
18 S. Kumar, S. Pola, C.-W. Huang, M. M. Islam, S. Venkateswarlu and Y.-T. Tao, *J. Org. Chem.*, 2019, **84**, 8562–8570.
19 Y. Dorca, C. Naranjo, P. Delgado-Martínez, R. Gómez and L. Sánchez, *Chem. Commun.*, 2019, **55**, 6070–6073.
20 Z. Zeng, Y. M. Sung, N. Bao, D. Tan, R. Lee, J. L. Zafra, B. S. Lee, M. Ishida, J. Ding, J. T. López Navarrete, Y. Li, W. Zeng, D. Kim, K.-W. Huang, R. D. Webster, J. Casado and J. Wu, *J. Am. Chem. Soc.*, 2012, **134**, 14513–14525.
21 T. Nishiuchi, S. Aibara, H. Sato and T. Kubo, *J. Am. Chem. Soc.*, 2022, **144**, 7479–7488.
22 A. Sánchez-Grande, J. I. Urgel, L. Veis, S. Edalatmanesh, J. Santos, K. Lauwaet, P. Mutombo, J. M. Gallego, J. Brabec, P. Beran, D. Nachtigallová, R. Miranda, N. Martín, P. Jelínek and D. Écija, *J. Phys. Chem. Lett.*, 2021, **12**, 330–336.
23 N. Martín, I. Pérez, L. Sánchez and C. Seoane, *J. Org. Chem.*, 1997, **62**, 870–877.

24 Y.-Q. Fang, O. Lifchits and M. Lautens, *Synlett*, 2008, **3**, 413–417.
25 U. Schubert, S. Hünig and A. Aumüller, *Liebigs Ann. Chem.*, 1985, **6**, 1216–1222.
26 E. Ortí, R. Viruela and P. M. Viruela, *J. Mater. Chem.*, 1995, **5**, 1697.
27 E. Ortí, R. Viruela and P. M. Viruela, *J. Phys. Chem.*, 1996, **100**, 6138–6146.
28 A. Savin, R. Nesper, S. Wengert and T. F. Fässler, *Angew. Chem., Int. Ed.*, 1997, **36**, 1808–1832.
29 J. Casado, K. Takimiya, T. Otsubo, F. J. Ramírez, J. J. Quirante, R. P. Ortiz, S. R. González, M. M. Oliva and J. T. L. Navarrete, *J. Am. Chem. Soc.*, 2008, **130**, 14028–14029.
30 V. Hernández, J. Casado, F. J. Ramírez, G. Zotti, S. Hotta and J. T. L. Navarrete, *J. Chem. Phys.*, 1996, **104**, 9271–9282.
31 C. Castiglioni, M. Gussoni, J. T. Lopez Navarrete and G. Zerbi, *Solid State Commun.*, 1988, **65**, 625–630.
32 R. L. Martin, *J. Chem. Phys.*, 2003, **118**, 4775–4777.
33 D. Wasserberg, S. C. J. Meskers, R. A. J. Janssen, E. Mena-Osteritz and P. Bäuerle, *J. Am. Chem. Soc.*, 2006, **128**, 17007–17017.